Chapter <mark>X</mark>

Nanomechanical Characterization of Soft Materials

A.H.W. Ngan

Abstract This Chapter reviews the creep or viscoelastic deformation behavior of soft materials under nanoindentation-type testing. Analysis protocols of nanoindentation based on the Hertzian elastic contact theory, linear viscoelasticity analyses, and a more recent rate-jump method, are described and assessed. In addition to continuous viscoelasticity, a special type of discrete creep deformation, often observed in a wide range of materials during nanomechanical testing, is also highlighted.

<mark>X</mark>.1 Introduction

The advent of nanomechanical techniques including atomic force microscopy (AFM) and nanoindentation has enabled mechanical behavior of materials of micron- and smaller sizes to be characterized. However, whereas the load-displacement responses are routinely measured by these experimental platforms, these need to be deconvolved in order to obtain intrinsic material parameters, such as elastic modulus and yield properties. Despite the continuous development of the hardware over the past three decades, this step remains to be very challenging, especially for soft materials which exhibit not only purely elasto-plastic but also time-dependent deformation. Yet, examples of such materials are ample in many fronts of today's technology, including polymers, gels, low-melting metals tested at room temperature or higher melting metals tested at elevated temperatures, and also biological tissues. This Chapter aims at to highlight some common experimental features and analysis methods concerning nanomechanical testing of soft materials that the author has experience with.

<mark>X</mark>.2 Common Data Analysis Protocols for Nanoindentation

Nanoindentation is the most mature nanomechanical characterization technique developed so far. Although nanoindentation was regarded as a special function of an AFM in the early days of development, as at today there are a few commercial suppliers selling stand-alone nanoindenter machines, while AFMs took a separate line of development. In such commercial nanoindenters, a diamond probe, usually a Berkovich tip, is sent down to the sample along a vertical travel axis, and nanoscopic force and displacement data are gathered, usually by a capacitor gage, during the indentation process on the sample. As mentioned above, the most

---

Department of Mechanical Engineering,
University of Hong Kong, Pokfulam Road, Hong Kong, P.R. China
Email: hwngan@hku.hk

challenging step, from a user's point of view, is to deconvolve the force-displacement data to obtain material properties. Here, some common data-analysis protocols are reviewed.
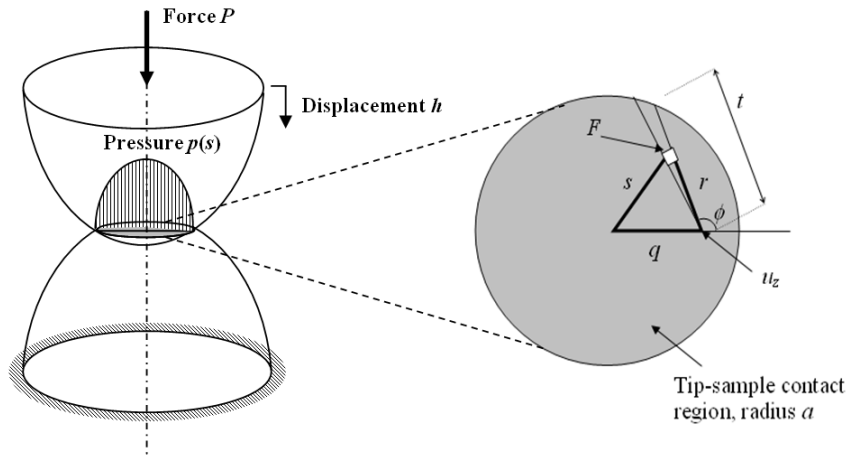

Figure X.1 Contact between two axi-symmetric elastic bodies

Oliver and Pharr (1992) proposed a procedure to analyze nanoindentation data which has become a standard protocol available in the software of all commercial nanoindenters nowadays. Their procedure is based on the Hertzian theory for elastic contact (Hertz 1882; Johnson 1999), and is applicable to an unloading event which is purely elastic. The Hertzian theory is also widely used for analyzing nanoindentation data from experiments carried out in an AFM, especially on biological samples (Lekka et al. 1999; Rosenbluth et al. 2006; Cross et al. 2007; Li et al. 2008). For these reasons, this theory is briefly outlined here. Figure X.1 shows the plan view of the contact area between two axi-symmetric elastic bodies, which represent the tip and the sample in the context of nanoindentation. A contact pressure distribution $p(s)$ is generated over this contact area, where s is the radial distance from the center. An infinitesimal area dA in this contact area is subjected to a point force $F = p(s)dA$ normal to the area, and from the theory of elastic stress potential of half-spaces (Johnson 1999), F produces a displacement field $u_z(r)$ on the surface of either contacting body along the direction of contact, according to

$$u_z(r) = \frac{(1-v^2)}{\pi E} \frac{F}{r} \ ,$$ (X.1)

where E and v are the Young modulus and Poisson ratio of the body, and r the radial distance from the position of F. Thus, by the principle of superposition in elasticity, the surface displacement of the body is the sum of contributions from all the point forces $F = p(s)dA = p(s)rd\phi dr$ arising from $p(s)$, and so is given by

$$u_z(q) = \frac{(1-v^2)}{\pi E} \int_{\phi=-\pi}^{\pi} \int_{r=0}^{t} p(s)drd\phi \ , \quad q < a.$$ (X.2)

In eqn. (X.2), q is the radial distance, from the center of the contact region, of the "field point" where u_z occurs, and a is the radius of the contact region. When applying eqn. (X.1) to eqn. (X.2), the infinitesimal area dA is taken as $dA = p(s)rd\phi dr$, where ϕ is the angular position of the "source point" (the point where F acts) from the field point (see Figure X.1), to take advantage that the r in dA and in eqn. (X.1) can get cancelled. The inner integral in eqn. (X.2) is from $r = 0$ to t, where $t = -q\cos\phi + \sqrt{a^2 - q^2\sin^2\phi}$, and s in $p(s)$ is given by $s^2 = r^2 + q^2 + 2rq\cos\phi$.

Suppose that the two elastic bodies, i.e. the specimen surface and the tip, are both spherical with radii of curvature R_1 and R_2 respectively ($R_1 \to \infty$ if the specimen surface is flat), so that for small values of q (see Figure X.1), the two surfaces are well approximated by $z_1 \approx q^2/(2R_1)$ and $z_2 \approx q^2/(2R_2)$ respectively. The deformation requires that $z_1 + u_{z1} + z_2 + u_{z2} = h$, where h is the relative displacement of the tip into the sample surface, and u_{z1} and u_{z2} are deformations of the specimen surface and the tip according to eqn. (X.2). Therefore, eqn. (X.2) becomes

$$h - \frac{q^2}{2R} = \frac{1}{\pi E_r} \int_{\phi=-\pi}^{\pi} \int_{r=0}^{t} p(s)drd\phi \tag{X.3}$$

where R and E_r, given by $1/R = (1/R_1) + (1/R_2)$ and $1/E_r = [(1-v_1^2)/E_1] + [(1-v_2^2)/E_2]$, are respectively a reduced radius and elastic modulus of the tip-sample contact. Hertz showed that the solution to eqn. (X.3) is $p(s) = p_o\sqrt{1-(s/a)^2}$, where $a = (\pi R p_o)/(2E_r)$ and $h = (\pi a p_o)/(2E_r)$ (Johnson 1999). The total indentation load is given by $P = \int_0^a 2\pi s\, p(s)ds = (2\pi p_o a^2/3)$. Key results of the Hertzian theory are therefore as follows:

$$a = \left(\frac{3PR}{4E_r}\right)^{1/3} ; \quad h = \frac{a^2}{R} = \left(\frac{9P^2}{16RE_r^2}\right)^{1/3} ; \quad p_o = \frac{3P}{2\pi a^2} = \left(\frac{6PE_r^2}{\pi^3 R^2}\right)^{1/3} . \tag{X.4}$$

The second equation in X.4 gives

$$P = \left(\frac{4}{3}\sqrt{R}E_r\right)h^{3/2} \tag{X.5}$$

and hence, the reduced modulus E_r can be obtained from a fit of the load-displacement curve to the form $P \sim h^{3/2}$, provided that R is known. This method of obtaining E_r is often used in nanoindentation experiments carried out in AFMs, and is in fact incorporated into the analysis software of some commercial AFMs. However, the underlying assumption is that the loading process is purely elastic.
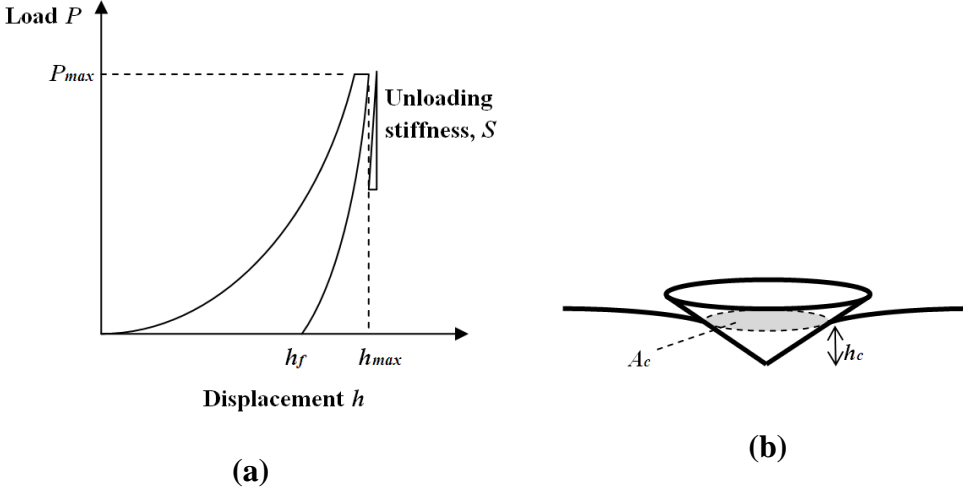
Figure X.2 (a) Schematic load-displacement graph and (b) sink-in morphology during nanoindentation.

In the Oliver-Pharr protocol (Oliver and Pharr 1992) adopted by commercial nanoindenters, whereas the loading process of a nanoindentation experiment can involve plasticity, the onset of a subsequent unloading process is assumed to be purely elastic (Figure X.2a). Under this assumption, the tip-sample contact stiffness S at the onset of unloading process, defined as $S = dP/dh$, is obtainable from the first two equations in (X.4) as

$$E_r = \frac{\sqrt{\pi}}{2} \frac{S}{\sqrt{A_c}} \tag{X.6}$$

where $A_c = \pi a^2$ is the projected area of the tip-sample contact circle (Figure X.2b). Thus, the elastic modulus E_r can be estimated if S and A_c are measured, and at the same time, the hardness can also be evaluated as $H = P_{\max}/A_c$. A_c is given from the contact depth h_c at full load, through a pre-calibrated tip-shape function $A_c = f(h_c)$, but because of the elastic "sink-in" deformation of the specimen's surface (Figure X.2b), h_c is not explicitly specified in the *P-h* curve. For a spherical indenter, geometry gives $h_c \approx a^2/2R_2$, and if the sample is initially flat, $R = R_2$, so that the indenter displacement at full load is $h_{\max} \approx a^2/R_2$ from the second equation in (X.4). Therefore, $h_c \approx h_{\max}/2$. However, this relation is valid only when the sample deforms purely elastically. In plastic indentation situations, Oliver and Pharr (1992) proposed that the corresponding plastic depth, h_f, should be deducted from the h data, i.e. instead of $h_c = h_{\max}/2$, we have

$$(h_c - h_f) = \frac{(h_{max} - h_f)}{2} \qquad\qquad\qquad \text{(X.7)}$$

Also, from the second equation in (X.4), $P \propto (h - h_f)^{3/2}$, and from this, the contact stiffness is given by

$$\frac{dP}{dh} = S = \frac{3}{2}\frac{P_{max}}{(h_{max} - h_f)} \cdot \qquad\qquad\qquad \text{(X.8)}$$

Combining eqns. (X.7) and (X.8), we have $h_c = h_{max} - (3/4)P_{max}/S$, for the case of a spherical tip indenting on a flat sample. Oliver and Pharr (1992) proposed the following more general formula:

$$h_c = h_{max} - \varepsilon \frac{P_{max}}{S}, \qquad\qquad\qquad \text{(X.9)}$$

where ε is a constant for a given indenter. Table X.1_new gives the values of ε for different indenter geometries.

Indenter shape	ε
Spherical and paraboloid	$\frac{3}{4} = 0.75$
Flat ended	1
Conical	$\frac{2}{\pi}(\pi - 2) = 0.73$

Table X.1 Values of ε in eqn. (X.9)

X.3 Viscoelastic Behavior during Nanoindentation

The analysis methods based on the Hertzian contact theory outlined above assume that the deformation is purely elastic in the relevant part of the load schedule. For soft materials, this condition is often not met, even during the unloading process. Figure X.3(a) shows a rather extreme case of nanoindentation carried out in amorphous selenium at 24°C (Tang and Ngan 2005), where the *P-h* curve bends forward during the initial part of the unload. This signifies significant creep deformation: the tip continues to sink into the specimen as it creeps under the tip load, even though the load on the tip is reducing. If the Oliver-Pharr method is applied to such a scenario, the resultant E_r would be negative as shown in Figure X.3(b), since the apparent contact stiffness S at the onset of unload is negative. The creep factor in Figure X.3(b) is defined as

$$C = \frac{\dot{h}_h S_{corr}}{|\dot{P}_u|}, \qquad\qquad (\text{X}.10)$$

where $\dot{h}_h$ is the creep rate at the end of the hold period just before the unload, S_{corr} is a corrected elastic contact stiffness (see eqn. (X.29)), and $\dot{P}_u$ is the unloading rate. As will be seen later, C measures the relative importance of elastic and creep deformation at the onset of the unloading process (Feng and Ngan 2002). The fact that creep is significant is also represented by a high value of $\dot{h}_h$ during the load-hold before unload, and in Figure X.3(a), this corresponds to a significant drop in the actual load applied onto the sample during the nominal load-hold stage prior to unload, due to the increasing spring force in the nanoindenter transducer as the tip sinks into the sample. Significant creep during unload, accompanied by a visible forward bending "nose" in the *P-h* curve, is a rather general behavior for soft materials, including polymers and biological (e.g. bone and cartilage) samples tested at room temperature, and even metals tested at high homologous temperatures relative to their melting points. Even though creep deformation may not be as severe as giving rise to an obvious "nose" in the *P-h* curve, it may still lead to significant overestimation of the contact stiffness S and hence the E_r estimated from the Oliver-Pharr analysis (Feng and Ngan 2002).

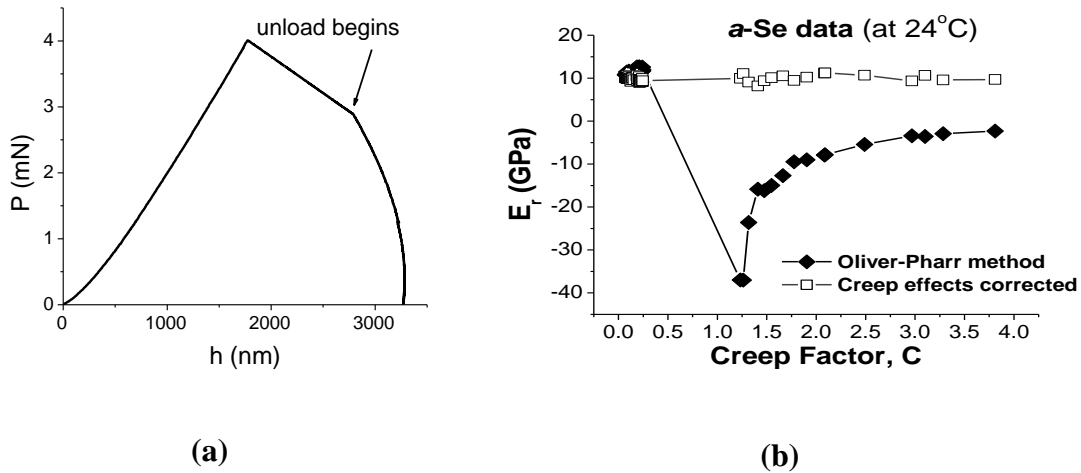(a)   (b)

Figure X.3. (a) A typical load-displacement curve in amorphous selenium at 311K. (b) Elastic modulus of amorphous selenium measured by the Oliver-Pharr method and after creep correction. Data from Tang and Ngan (2005).

As mentioned above, certain commercial AFMs are equipped in their analysis software with the Hertzian fit protocol involving eqn. (X.5), where the *P-h* curve measured during a load ramp is fitted with a $P \sim h^{3/2}$ law to obtain the E_r value. When creep or any time-dependent deformation occurs, the measured E_r would be dependent on the load ramp rate, as shown in Figure X.4(a) for the case of an oral cancer cell line indented by an AFM tip (Zhou et al. 2012). Similar rate-dependent results are often seen in the literature (e.g. Li et al. 2008), and their occurrence means that the measured properties are not intrinsic to the sample.
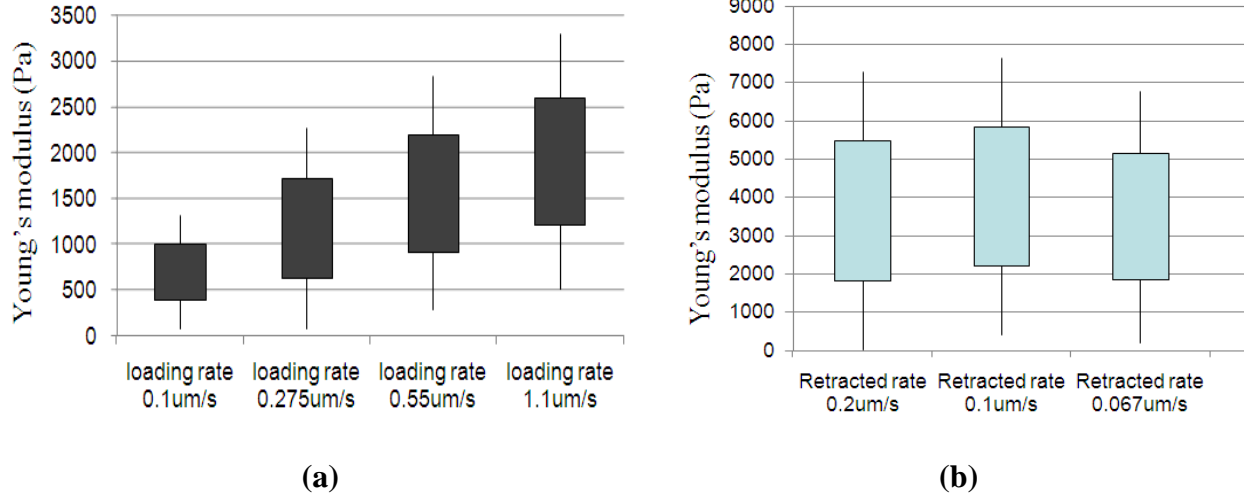
(a)   **(b)**

Figure X.4. Elastic modulus of UM1 oral cancer cells measured with (a) the Hertzian fit protocol in eqn. (X.5), (b) the rate-jump protocol in eqn. (X.5). Data from Zhou et al. 2012.

X.4 Linear Viscoelasticity Analyses of Nanoindentation

The viscoelastic behaviors commonly seen in nanoindentation of soft samples have been the subject of investigation by linear viscoelasticity analyses (Feng and Ngan 2002; Sakai 2002; Cheng and Cheng 2005; Oyen 2006). In one approach, nanoindentation is performed in a dynamic mode, involving a small oscillatory load $\Delta P = \Delta P_0 \, sin(\omega t)$ superimposed on the basic load. Because of viscosity, the displacement oscillation will in general exhibit a phase lag ϕ, i.e. $\Delta h = \Delta h_0 \, sin(\omega t - \phi)$. In analogy with eqn. (X.6), a storage modulus $E_r{}'$ and a loss modulus $E_r{}''$ can be defined as (Herbert et al. 2008):

$$E_r{}' = \frac{\sqrt{\pi}}{2\sqrt{A_c}} \frac{\Delta P_0}{\Delta h_0} \cos\phi \; ; \qquad E_r{}'' = \frac{\sqrt{\pi}}{2\sqrt{A_c}} \frac{\Delta P_0}{\Delta h_0} \sin\phi \, . \qquad (X.11)$$

While $E_r{}'$ and $E_r{}''$ are easily measured this way, they are usually strong functions of the oscillation frequency ω.

In a second approach, certain constitutive model is assumed as the intrinsic deformation law for the sample, and this is developed into measurables such as a *P-h* relation, which can then be fitted with the experimental data to obtain the coefficients in the model, which are supposed to be intrinsic material properties. Most viscoelasticity analyses carried out for nanoindentation made use of hereditary integrals (Sakai 2002; Cheng and Cheng 2005; Oyen 2006). Alternatively, another very useful technique is Radok's correspondence principle between linear viscoelasticity and elasticity (Radok 1957). As an illustration, consider the Maxwell model of viscoelasticity, with the following constitutive relation

7

$$\dot{e}_{ij} = \frac{1}{2G}\dot{S}_{ij} + \frac{1}{2\eta_s}S_{ij}, \quad \sigma_{ii} = 3B\varepsilon_{ii} \quad \text{(viscoelasticity).}$$ (X.12)

Here, $S_{ij} = \sigma_{ij} - \delta_{ij}\sigma_{kk}/3$ is the deviatoric stress, and $e_{ij} = \varepsilon_{ij} - \delta_{ij}\varepsilon_{kk}/3$ the deviatoric strain, G and B are the shear and bulk modulus respectively, and η_s is the shear viscosity. Laplace-transforming eqn. (X.12) leads to

$$e_{ij}^* = \left(\frac{1}{2G} + \frac{1}{2\eta_s}\cdot\frac{1}{s}\right)S_{ij}^*, \quad \sigma_{ii}^* = 3B\varepsilon_{ii}^* \qquad \text{(viscoelasticity)}$$ (X.13)

where $(\ )^*$ denotes the Laplace transform a time-dependent quantity $(\ )$, and s is the transform variable. Eqn. (X.13) is of a form analogous to Hooke's Law for a purely elastic material:

$$e_{ij} = \frac{1}{2G}S_{ij}, \quad \sigma_{ii} = 3B\varepsilon_{ii} \qquad \text{(elasticity);}$$

$$e_{ij}^* = \frac{1}{2G}S_{ij}^*, \quad \sigma_{ii}^* = 3B\varepsilon_{ii}^* \qquad \text{(elasticity).}$$ (X.14)

Comparing eqns. (X.13) and (X.14) suggests that the Laplace transform of the viscoelastic problem can be solved by replacing the elastic constants in the purely elastic problem by the following:

$$\frac{1}{G} \rightarrow \frac{1}{G} + \frac{1}{\eta_s}\cdot\frac{1}{s}; \quad B \rightarrow B.$$ (X.15)

The problem of indenting on a purely elastic half-space by a conical tip with semi-apex angle α has been solved by Sneddon (1965) (also c.f. eqn. (X.27)) as

$$\frac{1}{E_r}P(t) = \frac{2}{\pi}\tan\alpha\, h^2(t).$$ (X.16)

Since $E_r = 4G(3B+G)/(3B+4G)$, to obtain the corresponding P-h relation in the viscoelastic case, application of the transformations in eqn. (X.15) leads to the following transformation of E_r:

$$\frac{1}{E_r} \rightarrow \frac{1}{E_r} + \frac{1}{4\eta_s}\cdot\frac{1}{s} + \frac{E^2}{36B^2}\cdot\frac{1}{(3\eta_s s + E)}$$ (X.17)

where E is the Young's modulus. Therefore the Laplace transform of the viscoelastic version of eqn. (X.16) is

$$\left\{\frac{1}{E_r} + \frac{1}{4\eta_s}\cdot\frac{1}{s} + \frac{E^2}{36B^2(3\eta_s s + E)}\right\}P^* = \frac{2}{\pi}\tan\alpha\,(h^2)^*.$$ (X.18)

Inverse transforming eqn. (X.18) followed by differentiating with respect to t leads to

$$\frac{\dot{P}(t)}{E_r} + \frac{P(t)}{4\eta_s} + \frac{E^2}{108B^2\eta_s} \int_0^t \exp\left[-\frac{E}{3\eta_s}(t-t')\right]\dot{P}(t')dt' = \frac{2}{\pi}\tan\alpha\frac{d(h^2)}{dt} \tag{X.19}$$
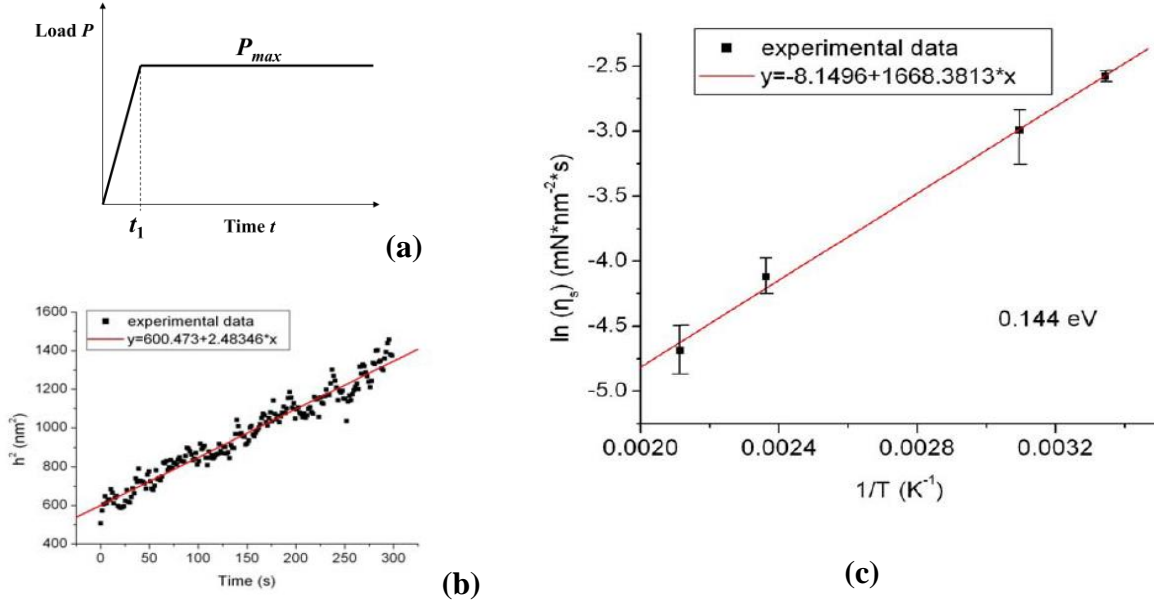
if $P(0) = 0$.

Figure X.5. Measurement of shear viscosity η_s in an amorphous Ge-Si alloy thin film. (a) Load schedule used. (b) h^2 vs t during load hold at P_{max}. (c) Arrhenius plot of η_s, exhibiting an activation energy of 0.14eV. Data from Xu (2008).

Numerical values indicate that the third term in eqn. (X.19) is usually small compared with the other two terms. When this third term is ignored,

$$\frac{\dot{P}(t)}{E_r} + \frac{P(t)}{4\eta_s} \approx \frac{2}{\pi}\tan\alpha\frac{d(h^2)}{dt}. \tag{X.20}$$

For a load-hold process up to P_{max} following a simple load ramp up to time t_1, as shown in Figure X.5(a), integrating eqn. (X.20) yields

$$h^2 \approx \frac{\pi P_{max}}{2\tan\alpha}\left[\left(\frac{1}{E_r} - \frac{t_1}{8\eta_s}\right) + \frac{t}{4\eta_s}\right] = a + bt \tag{X.21}$$

9

where a and b are constants. Figure X.5(b,c) show load-hold nanoindentation experiments carried out in an amorphous Ge-Si thin film (Xu 2008). The h^2 vs t plot is linearly in accordance with eqn. (X.21). The shear viscosity η_s can be obtained from the slope of the h^2-t plot, and data measured at different test temperatures obey an Arrhenius law as shown in Figure X.5(c), with an activation energy of ~0.14eV.

Constitutive models other than Maxwell can be similarly employed, and if more springs and dashpots are involved, more material constants will have to be obtained, and finding them can turn out to be a heavy curve-fitting exercise. Unfortunately, in most cases, there is simply no reliable guidance to help decide on which law is most suitable for a given material, yet the accuracy of such linear viscoelasticity analyses depends on the validity of the assumed constitutive law.

X.5 The Rate-jump Protocol of Nanoindentation

The linear viscoelasticity analyses mentioned above often yield storage ("elastic") or loss (viscous) coefficients which are supposed to be material properties on one hand, but on the other hand, are also strongly dependent of the test frequency, or rate of deformation in general. In the rheology literature, the rate dependence of such properties is accepted as "intrinsic" to the material itself, but in any case, this would still contradict the use of "springs" and "dashpots", supposedly with constant coefficients, in the constitutive law assumed. In an atomic model, the spring and dashpot elements in the correct constitutive law should correspond to the conservative stretching and permanent slippage or other dissipative events of the interatomic bonds in the solid, respectively. The spring elements of the viscoelastic network should therefore be characteristic of the nature and architecture of the atomic bonds in the solid, and truly material constants independent of the rate of deformation and other extrinsic factors.

A recent "rate-jump" protocol for carrying out mechanical tests in general has been proven to be capable of returning an intrinsic elastic modulus that is independent of the test conditions from viscoelastic materials (Ngan and Tang 2009). The key assumption of the constitutive law for the material is very mild – a network of any arrangement of (in general) non-linear viscous dashpots and linear elastic springs, as shown in Figure X.6(a), is assumed to hold within a very short time window $[t_c^-, t_c^+]$ about time t_c, at which a sudden step change in either the loading rate or the displacement rate, depending on whether the test is load- or displacement-controlled, is applied on the sample (Figure X.6(b)). The dashpots and springs here are described respectively by relations of the form

$$\dot{\varepsilon}_{ij}(\text{dashpot}) = \dot{\varepsilon}_{ij}(\sigma_{kl}), \tag{X.22}$$

$$\varepsilon_{ij}(\text{spring}) = s_{ijkl}\sigma_{kl} \tag{X.23}$$

where ε_{ij} and σ_{kl} are strain and stress tensors, and a dot above denotes time rate. Note that the $\dot{\varepsilon}_{ij}$ vs σ_{kl} relation in eqn. (X.22) is not necessarily linear (i.e. nonlinear viscosity is anticipated), and also, any arrangement of the springs and dashpots in the constitutive model is admissible. The latter two points are important differences with the linear viscoelasticity analyses described in the section above.
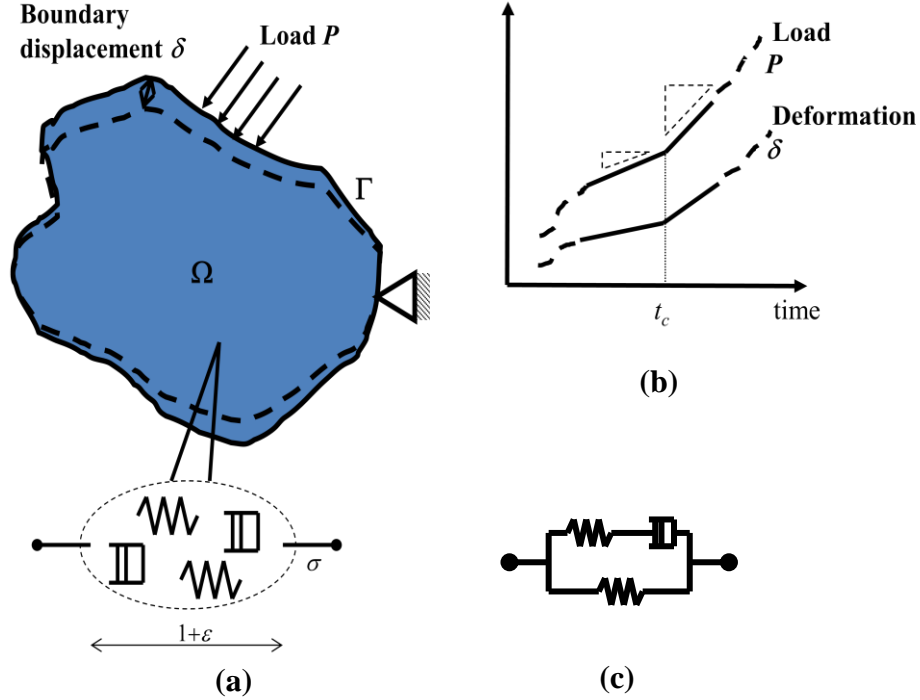

Figure X.6. (a) A general linear-elastic, nonlinear-viscous solid subjected to boundary load P undergoing deformation with boundary displacement δ. (b) Schematic of a rate jump in P and δ at time t_c. (c) An example of the viscoelastic network model of the material: the standard-linear-solid model, but any other network is admissible.

A key point to note about the nonlinear dashpots is that, by virtue of eqn. (X.22), a step change $\Delta\dot{\sigma}_{kl}$ in the stress rate field at t_c, arising from the step change in loading rate in Figure X.6(b), does not result in any non-zero change in the strain rate field $\dot{\varepsilon}_{ij}$ across the dashpots, because although the stress-rate $\dot{\sigma}_{kl}$ suffers a step jump $\Delta\dot{\sigma}_{kl}$, the stress itself must still be continuous across t_c. Thus, $\Delta\sigma_{kl} = 0$ across t_c, and from eqn. (X.22), $\dot{\varepsilon}_{ij}(\text{dashpot}) = 0$, i.e. the dashpots, whether they are linear or nonlinear and irrespective of their whereabouts in the constitutive network with respect to the springs, do not react to the rate-jump across t_c. Only the elastic springs react to the rate-jump according to eqn. (X.23), viz

$$\Delta\dot{\varepsilon}_{ij} = s_{ijkl}\Delta\dot{\sigma}_{kl}, \qquad (X.24)$$

and $\Delta \dot{\varepsilon}_{ij}$ and $\Delta \dot{\sigma}_{kl}$ are also the overall strain-rate and stress-rate changes of the sample across t_c. Eqn. (X.24) says that the fields $\Delta \dot{\sigma}_{ij}$ and $\Delta \dot{\varepsilon}_{ij}$ can be solved as a *linear elastic* problem, with the *same* elastic spring elements in the original viscoelastic model of the material while the dashpot elements are ignored.
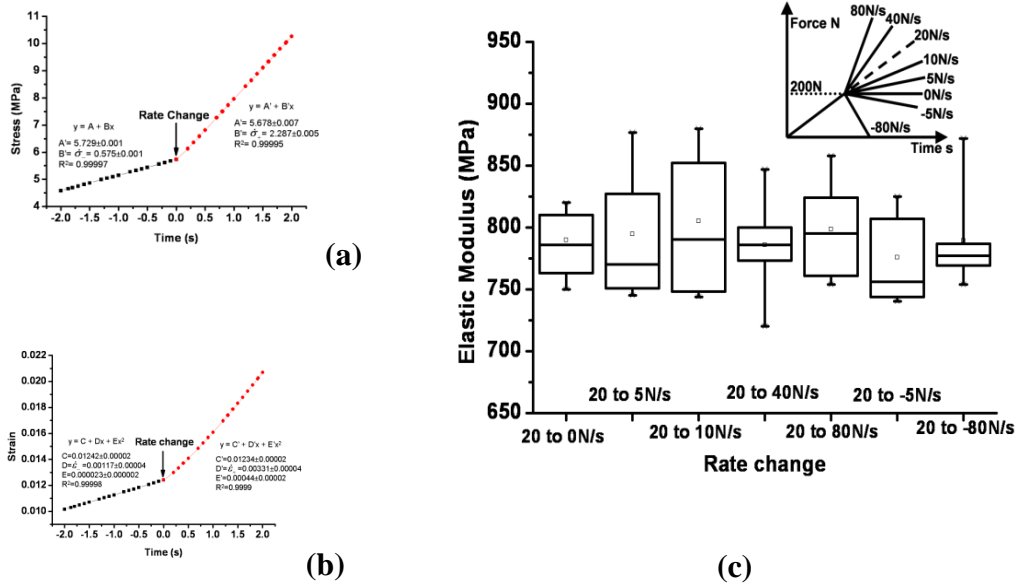

(a)

(b)

(c)

Figure X.7. Invariant effective modulus measured using the rate-jump protocol from tensile tests on high-density polyethylene. (a) Typical load schedule of nominal stress vs time with a rate jump imposed. (b) Response of nominal strain to the load schedule in (a). (c) *E* values calculated using eqn. (X.25) from different experiments with different magnitudes of load-rate jump. Inset in (c) shows the load schedules used. Data from Chan and Ngan (2010).

The solution of eqn. (X.24), for a given test geometry, would be a linear $\Delta \dot{P} \sim \Delta \dot{\delta}$ relation between the step changes in the load and displacement rates across t_c, with the linking proportionality constant being a lumped value of the elastic constants in the original viscoelastic model after removing all the dashpots. Fitting such a relation to experimental results allows this lumped value to be measured as an intrinsic elastic modulus of the material. As a simplest illustration, Figure X.7 shows results from macroscopic tensile tests performed on high-density polyethylene bars with such a rate-jump protocol applied (Chan and Ngan 2010). Figure X.7(a) shows a typical load schedule of nominal stress vs time, where a step change in the stress rate is imposed at time marked as 0. The corresponding nominal-strain response is shown in Figure X.7(b). From eqn. (X.24), an effective elastic modulus of the material is given by

$$E = \frac{\Delta \dot{\sigma}}{\Delta \dot{\varepsilon}} = \frac{\dot{\sigma}_+ - \dot{\sigma}_-}{\dot{\varepsilon}_+ - \dot{\varepsilon}_-} \qquad (X.25)$$

where $\dot{\sigma}_{+/-}$ and $\dot{\varepsilon}_{+/-}$ are the stress and strain rates, i.e. the slopes of the graphs in Figure X.7(a,b), measured before and after the rate jump and extrapolated to the latter. According to the above argument, E should be an intrinsic material constant independent of the test conditions. Figure X.7(c) shows the values of E measured using different magnitudes of load-rate jump, and it can be seen that E is indeed invariant.

In any test platform, eqn. (X.24) says that, provided that the load-displacement ($P \sim \delta$) relation for a *linear elastic* specimen during load-ramp is known, the corresponding $\Delta\dot{P} \sim \Delta\dot{\delta}$ relation for a viscoelastic sample can be obtained by the following simple substitutions:

$$\sigma \rightarrow \Delta\dot{\sigma} ;\ \varepsilon \rightarrow \Delta\dot{\varepsilon} ;\ P \rightarrow \Delta\dot{P} ;\ \delta \rightarrow \Delta\dot{\delta} ; \text{etc.} \tag{X.26}$$

In the following, we analyze nanoindentation as carried out in commercial nanoindenters, as well as in the AFM.

X.5.1 Rate-jump method in depth-sensing nanoindentation

In depth-sensing nanoindentation using the Oliver-Pharr protocol, the elastic modulus and hardness are evaluated at the onset of an unloading stage following a load-hold stage (e.g. see Figure X.3(a)). The onset point of unloading is therefore a rate-jump point pertinent to the above analysis. If the sample is purely elastic, the load-displacement relation is given by eqn. (X.6), i.e.

$$\frac{dh}{dP} = \frac{\sqrt{\pi}}{2E_r \sqrt{A_c}} . \tag{X.27}$$

Now, for a viscoelastic sample at the onset of unload, carrying out the substitutions in eqn. (X.26) in eqn. (X.27) gives

$$\frac{\Delta\dot{h}}{\Delta\dot{P}} = \frac{\dot{h}_h - \dot{h}_u}{\dot{P}_h - \dot{P}_u} = \frac{\sqrt{\pi}}{2E_r \sqrt{A_c}} , \tag{X.28}$$

where $\dot{h}_h$ and $\dot{h}_u$ are tip speeds just before and just after the unload onset point, and $\dot{P}_h$ and $\dot{P}_u$ are likely the load rates just before and after unload onset. The apparent contact stiffness, measurable as the slope of the *P-h* curve, is $S = \dot{P}_u / \dot{h}_u$, and writing $2E_r \sqrt{A_c / \pi}$ as S_{corr} the "correct" elastic stiffness, then a relation between S_{corr} and S can be obtained from eqn. (X.28) as

$$\frac{1}{S_{corr}} = \left(\frac{1}{S} - \frac{\dot{h}_h}{\dot{P}_u} \right) \times \frac{1}{\left(1 - \dot{P}_h / \dot{P}_u\right)} . \tag{X.29}$$

Eqn. (X.29) then serves as a correction formula for the viscous effects on the elastic contact stiffness (Feng and Ngan 2002; Ngan et al. 2005); the quantities needed for the correction include the creep displacement rate $\dot{h}_h$ and load drop rate $\dot{P}_h$ (due to the suspending springs in the transducer) at the end of the load hold prior to the unload, and the unloading rate $\dot{P}_u$ (<0), in addition to the apparent stiffness $S = dP/dh$ at the onset of unload. If the load-drop due to the suspending springs is negligible, then, with the creep factor defined in eqn. (X.10), the following can be obtained from eqn. (X.29):

$$\frac{S_{corr}}{S} \approx 1 - C \qquad (\text{X}.30)$$

which further indicates the effects of viscous deformation on the contact stiffness. In extreme cases (e.g. Figure X.3), C can be larger than unity, and then the apparent stiffness S will become negative. The corrected stiffness S_{corr} from eqn. (X.29) can be used to replace S in eqns. (X.6) and (X.9) to obtain the reduced modulus E_r and hardness as in the original Oliver-Pharr protocol (Feng and Ngan 2002; Ngan et al. 2005). Eqn. (X.29) also says that if the unloading rate $\dot{P}_u$ is very fast, or the hold before unload is very long so that $\dot{h}_h$ and $\dot{P}_h$ become very small, then correction is not necessary. However, knowing these conditions *a priori* would be difficult for very soft samples.
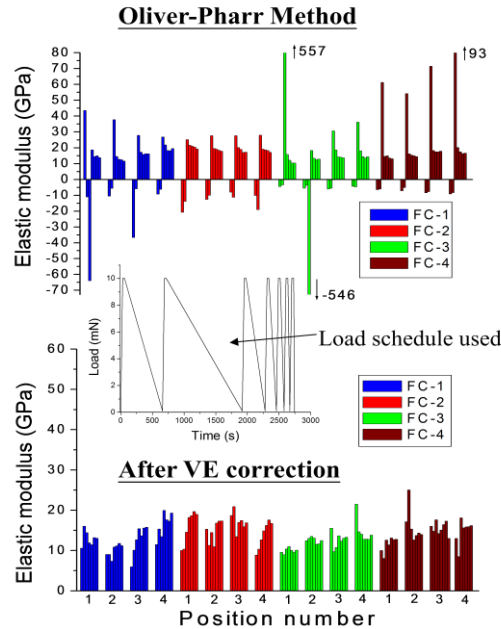

Figure X.8. The elastic modulus of mice cortical bone analyzed with the Oliver-Pharr method and rate-jump method. The inset shows the identical multi-cycle loading schedule for all the tests, in which the elastic modulus was calculated at the onset of each unloading portion. Data from Tang (2005) and Tang et al. (2006).

Figure X.8 compares the elastic modulus of mice cortical bone calculated with the rate-jump and the Oliver-Pharr protocols (Tang 2005; Tang et al. 2006). Here, a multi-cycle loading schedule was used to evaluate the elastic modulus at the onset of each unloading cycle. In the earlier cycles, the elastic modulus obtained by the Oliver-Pharr method becomes negative due to very severe viscoelastic effects, which lead to the "nose" phenomenon in the *P-h* curve (c.f. Figure X.3 for selenium). The rate-jump method is able to turn these cases back to normal with positive and rather consistent modulus values.

X.5.2 Rate-jump method in AFM nanoindentation

As mentioned earlier, nanoindentation is also routinely carried out in commercial AFMs, especially for testing biological tissues and nano-scale objects such as nano-filaments or wires. Compared with using a commercial depth-sensing nanoindentation machine, one major challenge arises in the AFM, namely, unlike the diamond Berkovich tips usually used in depth-sensing nanoindentation which are quite durable, AFM tips are much sharper and more fragile, and may not survive the many indentations required in obtaining the tip-shape function $A_c = f(h_c)$ (Figure X.2b) from a calibrating sample. In fact, the uncertain shape of AFM tips is one major disadvantage involved in the Hertzian fit protocol, since the tip-end radius R has to be known when applying eqn. (X.5). To avoid the damaging tip-shape calibration, flat-ended tips are recommended for AFM nanoindentation work (Figure X.9), and these can be easily made from commercial AFM tips by focused-ion-beam milling. The tip-sample contact size a (c.f. Figure X.1) then remains constant for different indentation depths, and a can be obtained easily by electron microscope imaging of the tip. Accurate determination of the initial contact point would also not be necessary since the contact size a is constant.
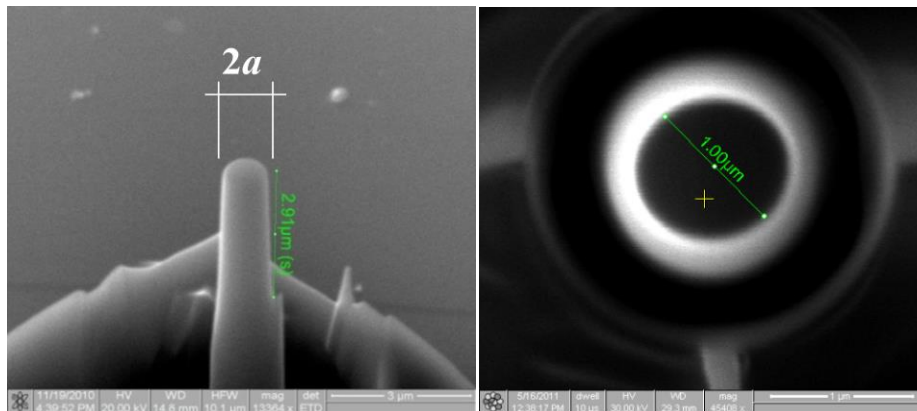

Figure X.9. Flat-ended tip for AFM nanoindentation, made by cutting a commercial tip by FIB milling (side view on left and top view on right; courtesy B. Tang)

As discussed above, the usual Hertzian fit method also gives rise to rate-dependent results in general, as illustrated in Figure X.4(a). The rate-jump protocol is definitely more attractive, as this should return an intrinsic elastic modulus of the sample. Figure X.10(a,b) shows two usual designs of commercial AFMs, one in which the tip-cantilever clamp is fixed and the sample moves up by displacement δ by piezoelectrics (Figure X.10a), and the other where the sample sits on a fixed platform while the cantilever clamp moves down by δ (Figure X.10b). In either case, the cantilever deflects with a displacement δ' at its free end, which is measured by a photo-diode. The cantilever deflection is related to the photo-diode signal D via a sensitivity constant A, i.e. $\delta' = AD$.

(a)   **(b)**
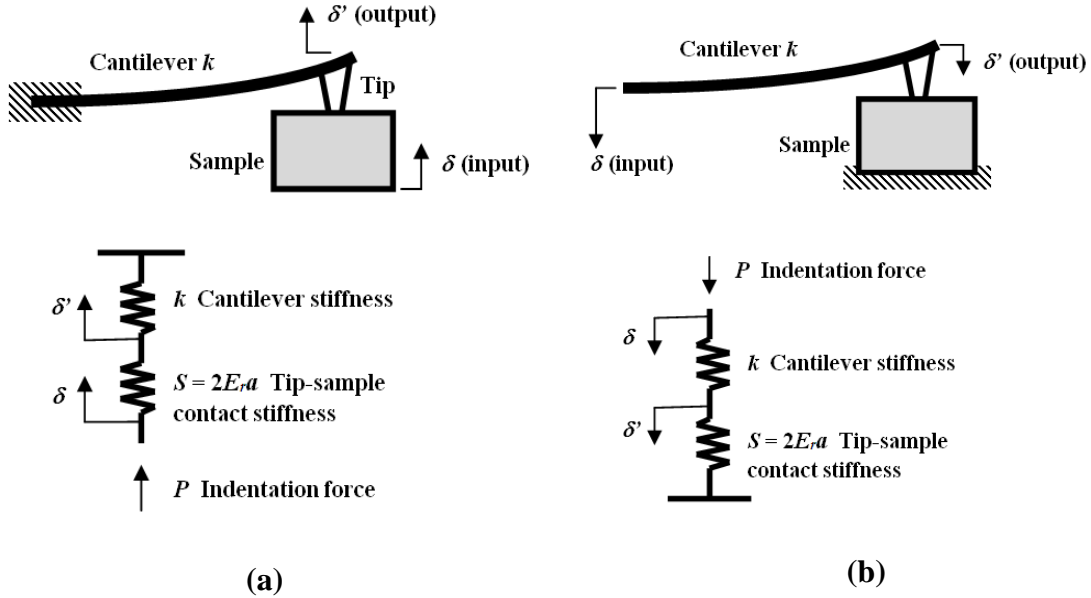
Figure X.10. Two designs of AFM. (a) Cantilever clamp fixed, sample moves up. (b) Cantilever clamp moves down, sample fixed.

For the first situation in Figure X.10(a), when the sample is purely elastic with tip-sample contact stiffness $S = 2E_r a$ (c.f. eqn. (X.6)), the indentation force is given by $P = k\delta' = S(\delta - \delta')$, where k is the force constant of the cantilever. This can be rearranged as $\delta/\delta' = (1 + \alpha/E_r)$, where $\alpha = k/2a$. For a viscoelastic sample under a rate-jump protocol, applying the substitutions in eqn. (X.26) gives

$$\frac{\Delta\dot{\delta}}{\Delta\dot{D}} = A\left(1 + \frac{\alpha}{E_r}\right), \qquad \text{(cantilever fixed, sample moves)} \qquad \text{(X.31)}$$

where $\Delta\dot{\delta}$ is an imposed step change in the movement rate of the sample base (i.e. the input), and $\Delta\dot{D}$ is the resultant step change in the rate of the photodiode signal D (the output).

For the second situation in Figure X.10(b) where the cantilever clamp moves, a similar analysis gives the following relation instead:

$$\frac{\Delta\dot{\delta}}{\Delta\dot{D}} = A\left(1 + \frac{E_r}{\alpha}\right) \qquad \text{(sample fixed, cantilever moves).} \qquad \text{(X.32)}$$

In either situation, the rate-jump relation eqn. (X.31) or (X.32) involves two machine constants, A the photo-diode sensitivity (i.e. cantilever deflection per unit sensor voltage or current generated), and $\alpha = k/2a$ which is a cantilever-tip constant, since both k and a are properties of the cantilever-tip. A also depends on the cantilever since different cantilevers will have different reflectivity for the laser. Thus, for a given cantilever-tip, if both A and α are pre-calibrated, eqn. (X.31) or (X.32) can be used to evaluate the E_r of an unknown specimen, by measuring the $\Delta\dot{D}$ for a step change $\Delta\dot{\delta}$ imposed at some point during the load schedule. To calibrate A and α, single indentations can be performed on two samples with known E_r values (e.g. one hard one soft), and A and α can then be obtained by solving two simultaneous equations of either (X.31) or (X.32) (Tang and Ngan 2011). This amount of calibration involving two single indentation tests should be the minimum required to achieve quantitative measurements by AFM nanoindentation, and tip damage can be minimized this way.

Figure X.4(b) shows the elastic modulus values measured from the same batch of oral cancer cells as in Figure X.4(a), using the above rate-jump protocol with three different rate-jump values of $\Delta\dot{\delta}$ (Zhou et al. 2012). The measured modulus does not exhibit any dependence on the magnitude of the $\Delta\dot{\delta}$ used, and so this is evidently an intrinsic constant of the cell line.

Referring back to Figure X.6(b), while the constitutive law involving eqns. (X.22) and (X.23) is expected to hold for a very short time span across the rate-jump time point t_c, for time- or strain-dependent materials, the constitutive law itself may evolve with time. For such materials, the effective elastic modulus measured from the rate-jump protocol would then be the material constant at t_c. Successive rate-jumps can be imposed along a load schedule to measure a series of E_r values along the strain path, and these should represent the evolution of the constitutive law or structure of the material over time or strain.

Although the rate-jump method is useful in returning an intrinsic elastic modulus of any viscoelastic sample, the viscous (dashpot) component of the deformation is subtracted out. The viscous component can only be obtained from linear viscoelasticity analysis of load-relaxation or creep response of the sample using an assumed constitutive model (see eqn. (X.21) and Figure X.5), or as the loss modulus by means of dynamic nanoindentation.

<mark>X</mark>.6 Discrete Yield Events in Soft Materials

Apart from smooth viscoelasticity or creep deformation, discrete plasticity events with time-dependent characteristics are also frequently observed in metals and polymers of small volumes. The first type of such discrete plasticity is delayed onset of yielding in well-annealed metals. It is well-known that annealed metals subjected to nanoindentation often exhibit discrete yield point, which marks the onset of plastic deformation. When the load is held at a value slightly below the yield point, no yielding or creep occurs initially as expected, but with prolonged application of load, a discrete yield event may occur suddenly after some waiting time, as shown by the example in Figure <mark>X</mark>.11. This waiting time is shorter as the load increases (Chiu and Ngan 2002), and for a fixed load, it exhibits a stochastic distribution (Figure <mark>X</mark>.11(b)). This delayed yielding behavior is thought to be due to thermally agitated nucleation of incipient dislocations within the stressed volume (Ngan et al. 2006).
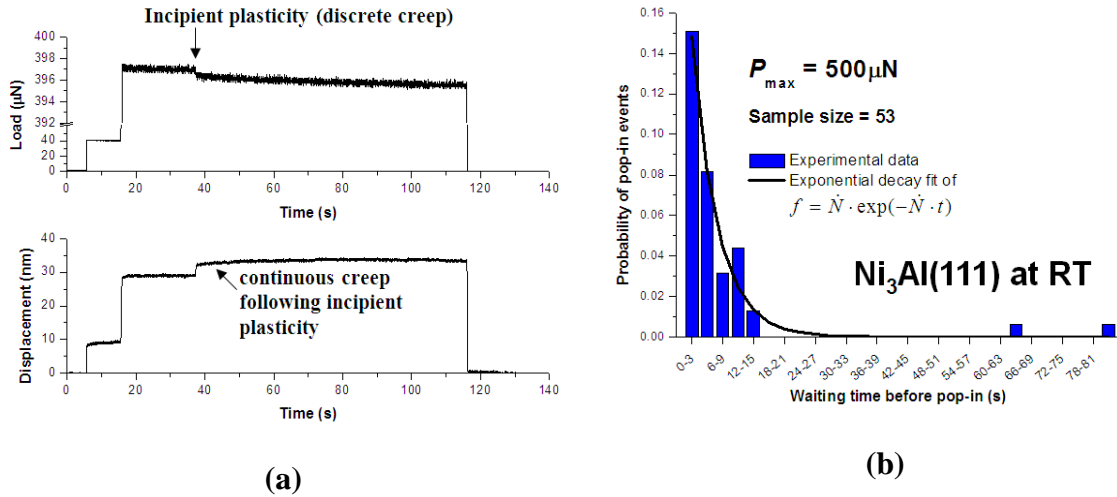

Figure <mark>X</mark>.11. Delayed incipient plasticity in Ni$_3$Al (111) during load-hold nanoindentation at room temperature. (a) Load and displacement versus time, showing the sudden occurrence of a discrete yield event during the load-hold. Creep follows immediately after the discrete event. (b) Statistical distribution of the waiting time for the discrete yield to occur at 500μN. Data from Wo et al. (2005).

Discrete plasticity is not confined to the onset of yielding, but can occur intermittently after first yield. Figure <mark>X</mark>.12(a) shows a type of creep deformation with discrete yield events in single-crystalline aluminum micro-pillars under uniform compression at room temperature (Ng and Ngan 2007). Figure <mark>X</mark>.12(b) shows a similar type of discrete creep, superimposed on smooth creep deformation, observed during constant-load nanoindentation on high-density polyethylene (Li and Ngan 2010). The occurrence frequency of the discrete creep events in polyethylene was

18

found to increase with crystallinity, suggesting that the discrete creep behavior is due to the crystal phases in the polymer. The discrete type of creep relaxation events represents an interesting contrast to the conventional smooth viscoelastic deformation, and is worthy of more investigations in the future.
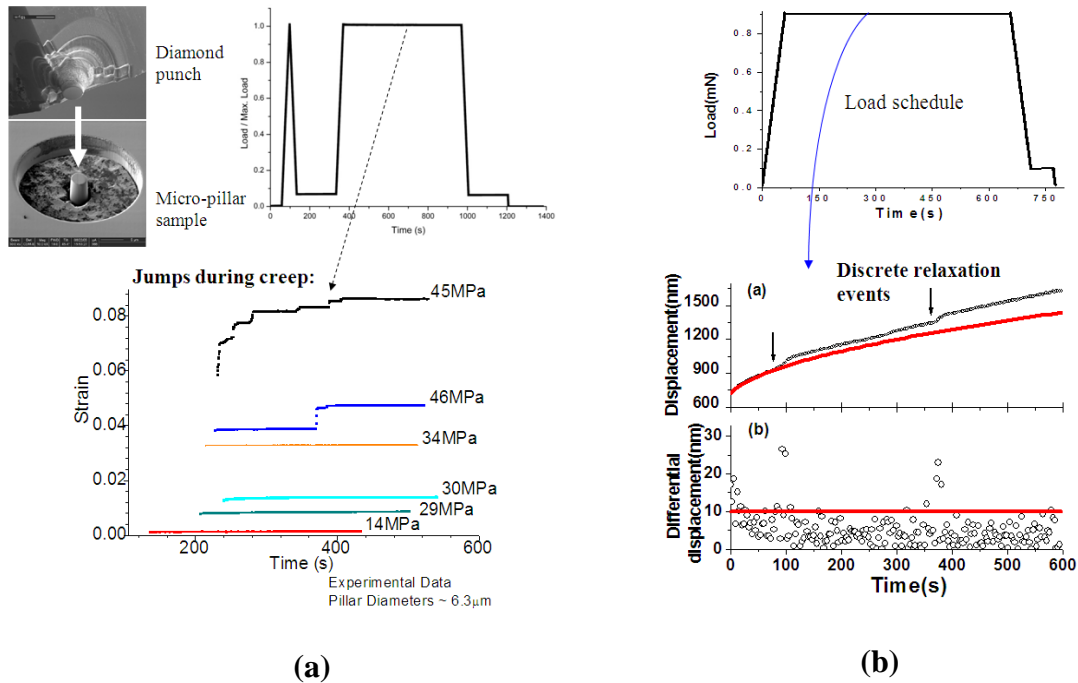

(a) **(b)**

Figure X.12. Successive discrete yield events during load-hold experiments. (a) Aluminum single-crystalline micro-pillars subjected to uniform compression at constant load at room temperature exhibit a type of creep deformation with discrete jumps (Ng and Ngan 2007). (b) High-density polyethylene subject to Berkovich nanoindentation at constant load at room temperature exhibits similar creep behavior with discrete jumps (Li and Ngan 2010).

X.7 Conclusions

In this Chapter, we have reviewed selected behavior and critical issues when soft materials are subjected to nanoindentation-type testing. Soft samples such as polymers, biological specimens, glasses approaching glass transition, and so on, often exhibit time-dependent viscoelastic deformation during nanoindentation testing. Data analysis protocols based on Hertzian-type theories are inadequate for such materials, often returning erroneous results. Linear viscoelasticity analyses are straightforward to carry out, but the choice of the suitable constitutive law is not an easy step, and such analyses often return rate-dependent storage and loss coefficients of the model, which is not ideal. A rate-jump protocol can return an intrinsic elastic modulus for any general linear-elastic, nonlinear-viscous solid, but no information can be

obtained concerning the viscous component of the constitutive law. In addition to continuous viscoelasticity, a wide range of materials also exhibit a discrete mode of creep deformation during nanomechanical testing.

References

Chan YL, Ngan AHW (2010) Invariant elastic modulus of viscoelastic materials measured by rate-jump tests. Polymer Testing 29:558-564.

Cheng YT, Cheng CM (2005) Relationships between initial unloading slope, contact depth, and mechanical properties for spherical indentation in linear viscoelastic solids. Mater. Sci. Eng., A 409:93-99.

Chiu YL, Ngan AHW (2002), Time-dependent characteristics of incipient plasticity in nanoindentation of Ni_3Al single crystal. Acta Mater. 50:1599-1611.

Cross SE, Jin YS, Rao J, Gimzewski JK (2007) Nanomechanical analysis of cells from cancer patients. Nat. Nano. 2:780–783.

Feng G. Ngan AHW (2002) Effects of creep and thermal drift on modulus measurement using depth-sensing Indentation. J. Mater. Res. 17:660-668.

Herbert EG, Oliver WC, Pharr GM (2008) Nanoindentation and the dynamic characterization of viscoelastic solids. J. Phys. D: Appl. Phys. 41:074021.

Hertz H (1882) Über die Berührung fester elastischer Körper, J. Reine Angew Math. 92:156-171.

Lekka M, Lekki J, Marszalek M, Golonka P, Stachura P, Cleff B, Hrynkiewicz AZ (1999) Local elastic properties of cells studied by SFM, Appl. Surf. Sci. 141:345–50.

Li JY, Ngan AHW (2010) Nano-scale fast relaxation events in polyethylene. Scripta Mater. 62:488-491.

Li QS, Lee GYH, Ong CN, Lim CT (2008) AFM indentation study of breast cancer cells. Biochem. Biophys. Res. Comm. 374:609–613.

Johnson KL (1999) Contact mechanics. Cambridge University Press, Cambridge.

Ng KS, Ngan AHW (2007) Creep of micron-sized aluminum columns. Phil. Mag. Lett. 87:967-977.

Ngan AHW, Wang HT, Tang B, Sze KY (2005) Correcting power-law viscoelastic effects in elastic modulus measurement using depth-sensing indentation. Int. J. Solids Strut. 42:1831-1846.

Ngan AHW, Zuo L, Wo PC (2006) Size dependence and stochastic nature of yield strength of micron-sized crystals: a case study on Ni_3Al. Proc. Roy. Soc. Lond. A 462:1661-1681.

Ngan AHW, Tang B (2009) Response of power-law-viscoelastic and time-dependent materials to rate jumps. J. Mater. Res. 24:853-862.

Oliver WC, Pharr GM (1992) An improved technique for determining hardness and elastic modulus using load and displacement sensing indentation experiments. J. Mater. Res. 7:1564-1583.

Oyen ML (2006) Analytical techniques for indentation of viscoelastic materials. Phil. Mag. 86:5625–5641.

Radok JRM (1957) Visco-elastic stress analysis. Q. App. Math. 15:198-202.

Rosenbluth MJ, Lam WA, Fletcher DA (2006) Force microscopy of nonadherent cells: a comparison of leukemia cell deformability. Biophys. J. 90:2994–3003.

Sakai M (2002) Time-dependent viscoelastic relation between load and penetration for an axisymmetric intenter. Phil. Mag. A 82:1841-1849.

Sneddon IN (1965) The relation between load and penetration in the axisymetric Boussinesq problem for a punch of arbitrary profile. Int. J. Engg. Sci. 3:47-57.

Tang B (2005) Nanoindentation of viscoelastic materials. PhD Thesis, University of Hong Kong.

Tang B, Ngan AHW (2005) Investigation of viscoelastic properties of amorphous selenium near glass transition using depth-sensing indentation. Soft Mater. 2:125-144.

Tang B, Ngan AHW (2011) Nanoindentation using an atomic force microscope. Phil. Mag. 91: 1329-1338.

Tang B, Ngan AHW, Lu WW (2006) Viscoelastic effects during depth-sensing indentation of cortical bone tissues. Phil. Mag. 86:5653-5666.

Wo PC, Zuo L, Ngan AHW (2005) Time-dependent incipient plasticity in Ni_3Al as observed in nanoindentation. J. Mater. Res. 20:489-495.

Xu ZW (2008) Phase transformation and properties of magnetron sputtered GeSi thin films. PhD Thesis, University of Hong Kong.

Zhou ZL, Ngan AHW, Tang B, Wang AX (2012) Reliable measurement of elastic modulus of cells by nanoindentation in an atomic force microscope. J. Mech. Behav. Biomed. Mater. 8:134-142.